PHYSICAL REVIEW APPLIED **21,** 054029 (2024)

Editors' Suggestion

Acoustically driven single-frequency mechanical logic

Erick Romero,[†] Nicolas P. Mauranyapin,[†] Timothy M.F. Hirsch, Rachpon Kalra, Christopher G. Baker, Glen I. Harris, and Warwick P. Bowen[*]

School of Mathematics and Physics, The University of Queensland, Queensland 4072, Australia

(Received 12 July 2023; revised 18 February 2024; accepted 15 March 2024; published 15 May 2024)

Nanomechanical computers promise robust, low-energy information processing; however, to date, electronics have generally been required to drive gates, and logical operations have generally involved bits with different oscillation frequencies. This limits the scalability of nanomechanical logic. Here we demonstrate an acoustically driven logic gate that has a single frequency of operation. Our gate uses the bistability of a nonlinear mechanical resonator to define logical states. These states are efficiently coupled into and out of the gate via nanomechanical waveguides, providing the mechanical equivalent of electrical wires and allowing purely mechanical information transfer. Since the inputs and output all share the same frequency, they are compatible with cascaded chains of gates. Our architecture is CMOS compatible, and with miniaturization could allow an energy cost that approaches the fundamental Landauer limit. Together this presents a pathway towards large-scale nanomechanical computers.

DOI: 10.1103/PhysRevApplied.21.054029

I. INTRODUCTION

The miniaturization of semiconductor electronics has fueled remarkable progress in computer performance over more than six decades; however, this progress has now markedly slowed [1,2]. Thermal fluctuations of the energies of electrons and holes are a key barrier. Known as *Boltzmann's tyranny* [3], they enforce a minimum supply voltage for error-free computation that constrains the energy cost of logic operations to approximately 30 aJ [3–5]. This is a factor of 10^4 higher than the fundamental Landauer limit, which arises from the creation of entropy when information is erased in irreversible computing [2,6]. Semiconductor electronics are also susceptible to degradation in harsh conditions, such as high-temperature and radiation environments [7,8]. This imposes challenges for applications in space and in medical and nuclear facilities, and in fields such as geothermal exploration and advanced propulsion systems [8].

In nanomechanical computing, information is encoded in mechanical motion rather than electrical charge [9]. This evades Boltzmann's tyranny, in principle allowing the Landauer limit to be reached [10], and affords intrinsic robustness with regard to radiation and high temperature [11,12]. Nanomechanical computers also offer new computing modalities, such as adaptive information processing, where the computer directly interacts with its environment via forces that it exerts or that are exerted upon it [13]. These qualities, together with rapid advances in nanofabrication, have provided the impetus for much recent progress, including nanomechanical computers built from metamaterials [12,14] and DNA origami [15,16], emulation of emergent phenomena such as ferromagnetism [17] and symmetry breaking [18], and reversible mechanical computing [19]. Nanomechanical elements are now even being applied as memories and interfaces for quantum computers [20–22]. However, scaling nanomechanical gates into complex circuits remains an outstanding challenge.

Unlike nanoelectromechanical computing, where information is stored in a combination of mechanical motion and electrical charge [23–25], scalable computer architectures that store information purely in mechanical degrees of freedom have yet to be developed. Purely mechanical gates generally rely on parametric interactions between mechanical waves [26–28], but these shift the frequencies of the bits, so the output of one gate cannot easily be used as the input of the next. Alternatively, direct physical contact has been used to interconnect nanomechanical gates [16] but, lacking the equivalent of nanomechanical wires, this is constrained to simple circuit topographies.

Here we report a single-frequency nanomechanical logic gate that accepts logical information stored purely in acoustic waves and is able to perform universal logic. Our gate has a mechanical quality factor 2 orders of magnitude higher than that of previous nanomechanical gates [10,19,27,29]. It is connected to nanomechanical waveguides that act as wires for the input and output bits, and it could therefore be used in the future to interconnect gates

[*]Corresponding author: w.bowen@uq.edu.au

[†]These authors contributed equally to this work.

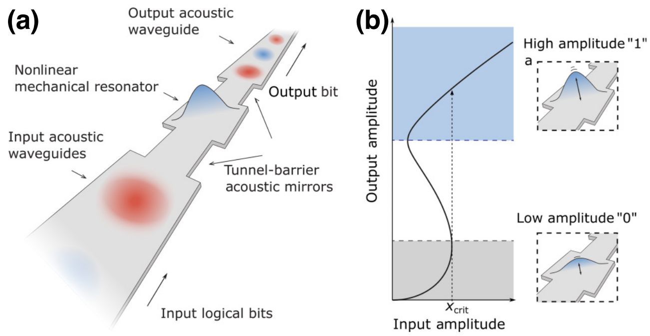

FIG. 1. Concept of acoustically driven nanomechanical logic. (a) The nanomechanical gate is based on a nonlinear mechanical resonator that is created by our placing two tunnel-barrier acoustic mirrors within a single-mode acoustic waveguide. The gate can be precisely coupled to input and output waveguides by our controlling the length of the tunnel barriers. (b) Gate operations are implemented with use of the bistability of the resonator, which results in an abrupt jump from a “0” state to a “1” state at a critical input amplitude x_{crit}.

[30]. We show that acoustic input bits can be coupled into the gate with 99% efficiency and that they can drive transitions between two bistable states [31–33]. This enables an approach to nanomechanical computing [34] for which we demonstrate a universal set of purely mechanical logic operations. Importantly, the output bits have the same frequency as the inputs and are therefore compatible with downstream gates. Our approach is CMOS compatible and our modeling suggests that the Landauer limit could be reached with miniaturization. While significant technical challenges remain, this provides a pathway towards highly efficient, robust computer processing.

II. ARCHITECTURE

Our nanomechanical computing architecture is constructed on a silicon chip by our combining single-mode acoustic waveguides [32] with evanescent tunnel barriers [Fig. 1(a)]. The tunnel barriers are created by our locally narrowing the width of the waveguide until it no longer supports any acoustic modes. Previous work has shown that such tunnel barriers can function as acoustic mirrors with reflectivity that can be finely tuned by control of their length in fabrication [35]. Here we use pairs of closely separated tunnel barriers to create an acoustic resonator reminiscent of an optical Fabry-Perot cavity. These resonators form the nanomechanical logic gates in our computing architecture. Acoustic logical bits are input and output as acoustic pulses that propagate within the single-mode acoustic waveguides. The logic operations and the flow of logical bits are therefore purely mechanical, with electronics used only to initialize and energize the system.

Our acoustic resonators exhibit a strong hardening Duffing nonlinearity that introduces a bistability in the oscillation amplitude [36]. This causes an abrupt transition from low to high amplitude when the input acoustic wave reaches a critical amplitude [Fig. 1(b)]. Electrically driven, this transition has been used to implement a nanomechanical memory [23]. Its use for nanomechanical logic was suggested recently [34], with the major advantage that the input and output logical bits have near-identical spatiotemporal properties, so the output of one gate can be used as the input for the next. We follow this approach here, defining the low-amplitude and high-amplitude states, respectively, as the logical “0” and “1” states.

III. EXPERIMENT

The physical platform for our nanomechanical logical architecture uses a CMOS-compatible *mesh-phononic* approach that we developed previously [35]. Here we fabricate an array of 80-nm-thick, 80-μm-square mechanical resonators from a stressed silicon nitride membrane (see Fig. 6). Each resonator is connected through evanescent tunnel barriers to single-mode input and output waveguides. Figure 2, for example, shows a chip containing eight waveguide-coupled resonators, each with different tunnel-barrier lengths. The factor-of-1000 aspect ratio between the size of a resonator and the thickness of the film results in a strong geometry-induced Duffing nonlinearity, reducing the energy required for logic operations (see Appendix B). Gold electrodes are patterned on the input waveguide. We use these to generate the acoustic inputs to each logic gate.

The input acoustic logical bits to our nanomechanical logic gate, which we refer to as A and B, are introduced by electric forces between a ground plate situated at the bottom of the chip and two of the electrodes situated on the input acoustic waveguide (see Fig. 3). The third electrode is used to provide a pump acoustic wave P that drives the nanomechanical gate close to the nonlinear Duffing transition. This provides gain for logic operations, amplifying the amplitude of the output bit relative to the inputs and therefore offsetting any attenuation that might occur in propagation between logic gates. A combination of a dc voltage and a voltage oscillating at frequency Ω, close to the natural resonance frequency of the mechanical resonator Ω_m, is applied between each electrode and a ground plane under the chip (see Fig. 3). Since the electric force scales as the voltage applied squared, the simultaneous application of an ac voltage and a dc voltage leads to a force proportional to $V_{\mathrm{dc}}^2 + 2V_{\mathrm{dc}}V_{\mathrm{ac}} + V_{\mathrm{ac}}^2$. Thus, the response at the drive frequency Ω (proportional to $2V_{\mathrm{dc}}V_{\mathrm{ac}}$) is boosted by a factor of $2V_{\mathrm{dc}}/V_{\mathrm{ac}}$ compared with the sole response at 2Ω (proportional to V_{ac}^2) present when no dc bias is applied. This results in three spatially separated forces on the waveguide, $F_j = a_j \cos(\Omega t + \phi_j)$ [32,35],

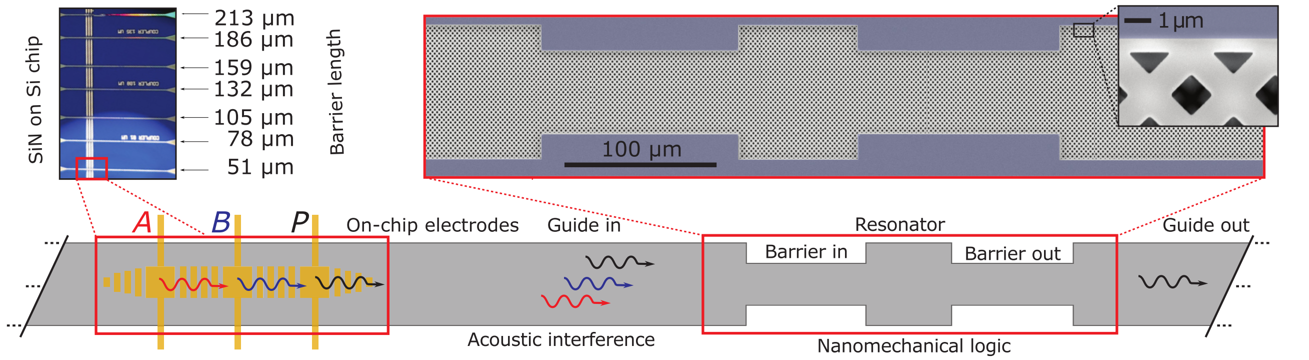

FIG. 2. Fabricated nanomechanical computing architecture. Top: The nanomechanical logic architecture, showing the on-chip electrodes, acoustic interference, and nonlinear mechanical resonator. Bottom: Microscope images of fabricated components. Left: Optical microscope image of the device chip, showing eight logic devices. Middle and right: Scanning electron micrographs of the on-chip electrodes (false color) and nanomechanical resonator. To minimize acoustic impedance mismatch, and therefore reflections, gold strips are deposited both between and on either side of the electrodes, with the length of the strips on the sides gradually tapered to zero to create an adiabatic transition to the bare acoustic waveguide (see Appendix A). The inset shows a magnified image of the silicon nitride meshed structure.

where $j \in \{A, B, P\}$ labels the electrodes that each force is applied to and a_j and ϕ_j are the amplitude and phase of the force. These forces generate out-of-plane acoustic waves that propagate along the input waveguide and interfere with each other to produce the combined acoustic input to the nanomechanical logic gate. In the future, independent waveguides could be used for each input, either separately driving the logic gate or combined acoustic signals on an acoustic beam splitter before it.

The electrodes and ground plane are separated by the roughly 0.5 mm thickness of the silicon chip. Since capacitive forces are roughly inversely proportional to the square of the separation [37], this configuration would usually require a potential difference on the order of kilovolts to

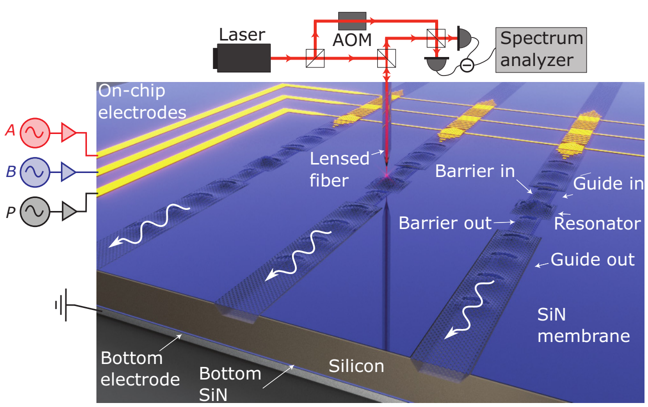

FIG. 3. Experimental setup for acoustically driven nanomechanical logic. Devices are actuated with electric capacitive forces between three individual on-chip electrodes A, B, and P and a bottom electrode situated below the chip. Motion of the silicon nitride membrane is detected with a custom-built vibrometer combining a lensed fiber with heterodyne detection and recorded on a spectrum analyzer.

deflect the waveguide enough to access nonlinear oscillation amplitudes (see Appendix D). However, by choosing a boron-doped silicon substrate, which exhibits extremely high permittivity [38,39], we are able to effectively displace the ground-plane potential to the top of the silicon substrate, around 1 μm away from the on-chip gold electrodes. This increases the capacitive forces by more than 5 orders of magnitude, reducing the required potential difference to as little as tens of volts, as shown in the next section.

IV. RESULTS

A. Nonlinear resonator

To detect the motion of the mechanical resonator, we use a custom-built laser vibrometer based on a combination of a lensed fiber and heterodyne measurement [32,35], as described in Appendix E. As a first test, we observe the thermal motion of seven nanomechanical resonators, each with different tunnel-barrier lengths and therefore different quality factors. The input and output tunnel-barrier lengths are chosen to be equal. In the absence of intrinsic dissipation, this forms an impedance-matched acoustic cavity such that a resonant input acoustic wave is fully transmitted through the resonator and into the output waveguide. An example measurement of the power spectral density of a nanomechanical resonator with a barrier length of 105 μm is displayed in Fig. 4(a). The mechanical resonance frequency $\Omega_m/2\pi = 4.13$ MHz agrees well with our predictions based on finite-element modeling (see Appendix B).

The ability to engineer the waveguide-resonator coupling enables wide tunability of both the resonator quality factor and transmission. Figure 4(b) shows the loaded mechanical quality factors extracted from power spectra

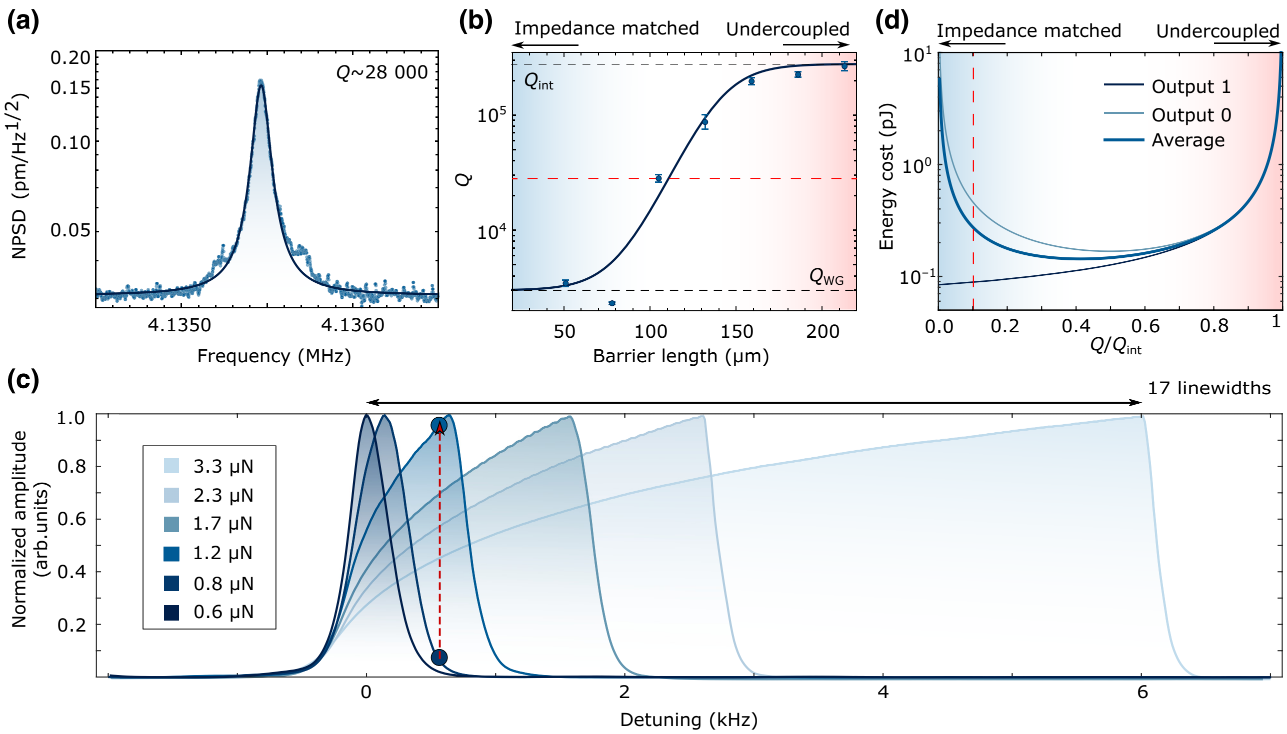

FIG. 4. Purely acoustic driving of nanomechanical logic gates. (a) Experimental measurements of the thermal noise power spectral density (NPSD) of a resonator with $Q \sim 28\,000$. (b) Loaded quality factor as a function of the length of the acoustic mirrors. (c) Normalized response of the nanomechanical meshed resonator to a swept-frequency acoustic tone. As the driving force is increased, the response becomes increasingly skewed, characteristic of a Duffing nonlinearity. At 660 Hz blue detuned from resonance, the data points connected by a dashed red arrow show the sharp transition from a logical “0” to a logical “1” when the drive force is increased from 0.8 to 1.2 μN. (d) Predicted energy cost of logical operations as a function of loaded quality factor. The dashed red arrow indicates the predicted energy cost for our loaded quality factor of 28 000. The parameters and equations used for these results are summarized in Table I.

for each of the seven measured resonators. For barrier lengths greater than 150 μm, the quality factor saturates at the unloaded quality factor of the resonator, which we find to be $Q_{\mathrm{int}} = 275\,000$, around 2 orders of magnitude higher than what has previously been reported for a nanomechanical gate [10,19,27,29]. At barrier lengths less than 50 μm, the quality factor instead approaches $Q_{\mathrm{WG}} \sim 3000$, bounded above zero because of reflections at the ends of the waveguides. Apart from one resonator, for which a dust particle was observed on the meshed-membrane (barrier length of 78 μm), we find that the transition between the two regimes agrees well with modeling.

A key development in our work is the ability to drive a nanomechanical resonator into the bistable regime through an acoustic waveguide. To explore this we drive the pump electrode P on the input waveguide to introduce an acoustic wave. Sweeping the acoustic frequency through the nanomechanical resonance frequency from below, we monitor the resonator amplitude in response to the acoustic wave and observe the skewed Lorentzian response characteristic of a hardening Duffing resonator [40]. Figure 4(c) shows the response of a resonator with a measured loaded quality factor Q of 28 000 (tunnel-barrier length of 105 μm) for a range of drive forces. We find that the bistable regime, where the resonance curve is multivalued, is reached for a combination of a dc voltage and a peak ac drive voltage as low as 30 V and 0.09 V, respectively. This corresponds to a force F at frequency Ω of 94 nN, with $F = \epsilon_0 A V_{\mathrm{dc}} V_{\mathrm{ac}}/d^2$ [32], where ϵ_0 is the vacuum permittivity, $A = (63\ \mu\mathrm{m})^2$ is the electrode area, and $d = 1\ \mu\mathrm{m}$ is the effective distance between the waveguide electrode and the bottom electrode.

As shown by the vertical red arrow in Fig. 4(c), at a fixed detuning of 660 Hz an abrupt transition occurs from low to high amplitude at a drive strength of 94 nN. In our computing scheme, these low-amplitude and high-amplitude states correspond to the logical “0” and “1” states.

Finite-element simulations provide a nonlinear Duffing coefficient α of 2.6×10^{13} N/m^3 for the resonator (see Appendix B). From this we calculate a critical energy $E_{\mathrm{crit}} = k^2/3\alpha Q$ to reach the bistable regime required for computing of 28 fJ (see Appendix F), where $k = 253$ N/m is the linear spring constant of the resonator. This roughly defines the minimum energy cost of a gate operation with our architecture and is comparable to the energy cost of a gate in a 1995 Pentium Pro semiconductor microprocessor [41]. In practice, the energy cost depends on whether the output is a "0" or a "1," since the lower amplitude of a "0" means the gate must reject more of the input energy in this case. It also depends on the duration of the logical pulses and the amplitudes of the logical bits, among other factors. We model the energy cost for both "0" and "1" outputs (see Appendix G) using our experimental parameters. The results are shown as a function of the loaded quality factor in Fig. 4(d), along with their average. The minimum average energy cost of 124 fJ is predicted to occur for a loaded quality factor Q of approximately $0.41Q_{\mathrm{int}}$. For technical reasons, we choose to work with a device for which $Q \sim 0.1Q_{\mathrm{int}}$ ($Q = 28\,000$), corresponding to a mechanical decay time $\tau = 2\pi Q/\Omega_m$ of 7 ms. This results in a somewhat higher average energy cost of 240 fJ [dashed red line in Fig. 4(d)], but increased efficiency of transmission into the output waveguide. We were unable to experimentally confirm this because the transmission was significantly modified by acoustic resonances caused by reflections from the end of the output waveguide. Nevertheless, we are able to infer the transmission from the experimentally determined loaded and unloaded quality factors [Fig. 4(b)]. We find on-resonant input acoustic waves are transmitted into the gate with 99% efficiency and into the output waveguide with 81% efficiency (see Appendix C).

B. Nanomechanical logic

To demonstrate nanomechanical logic, we drive the A, B, and pump P electrodes on the input waveguide with logic pulses. This creates 120-ms acoustic pulses, temporarily separated by a delay of 200 ms, that are synchronized to interfere with each other as they propagate, before the nanomechanical resonator (see Fig. 2). The pulses have a rectangular envelope and the same carrier frequency Ω (see Appendix H). Careful choice of their phases and amplitudes enables a full set of Boolean logic gates to be implemented within the nanomechanical resonator. As an example, in Fig. 5 we demonstrate a universal NAND gate using a nanomechanical resonator with $Q \sim 28\,000$. Here, the pump acoustic wave P is chosen to have an amplitude that is high enough to drive the nanomechanical logic gate beyond the critical amplitude $x_{\mathrm{crit}} = \sqrt{2k/3\alpha Q} = 15$ nm (see Appendix F) on its own, and into the "1" state with an oscillation amplitude greater than 18 nm [shown in the purple-filled pulse in Fig. 5(a), where both inputs A and B are zero]. The A and B logical inputs are arranged to be out of phase with the pump, destructively interfering with it. Their amplitudes are chosen so that the nanomechanical logic gate transitions to the "0" state (with an oscillation amplitude below 2 nm) only if both A and B inputs are "1"s. To reinitialize the system after logic operations, the drives are switched off so that the resonator rings down to its thermal amplitude [see Fig. 5(a)]. When the next set of pulses arrives, the resonator then rings up to reach a "0" or "1" state as described in Fig. 1(b) without the need for the drive-frequency sweep that is often used to initialize Duffing resonators.

For Fig. 5, we drive the gate with a sequence of all possible input combinations ("00," "01," "10," and "11"), which allows us to record the truth table of the NAND gate in a single measurement of the peak of the nanomechanical power spectral density over time. As can be seen, the NAND gate operates as expected: the "00", "01," and "10" acoustic inputs all result in a "1" output state, while a "11" input results in a "0" output state. Similar performance was achieved in earlier experiments for XOR, AND, and NOR gates (see Appendix H). From the measured amplitude of motion of the resonator, its quality factor, and the resonator-drive detuning, our model gives an average gate energy cost of 240 fJ as described above. We also performed faster gate operations, reducing the operation time from the 120 ms shown in Fig. 5 to as short as 10 ms, slightly longer than the decay rate of the nanomechanical resonator. This reduced the average gate energy cost to 20 fJ.

C. Error statistics and fatigue

We repeated the sequence of four possible sets of input states ("00," "01," "10," and "11") more than 1500 times without any adjustment of the amplitude and phase of A, B, and P drive, and we observed no failures of gate operations. We tested for mechanical fatigue by pumping a logic gate continuously for 2 months, observing no statistically significant changes in mechanical quality factor or nonlinearity.

To investigate the statistical probability of a failure, we correct for slow thermal drifts in the output amplitude and compute histograms of this normalized amplitude for each of the four sets of input states, as described in Appendix I. As shown in Fig. 5(b), the amplitude fluctuations are far smaller than the separation of the "0" and "1" output states, consistent with our observation of no errors over the full sequence of measurements. Indeed, we find that the separation between the "0" bit value (red trace) and the lowest "1" bit value (blue trace) corresponds to approximately 10^7 times the characteristic thermal energy, $k_B T$, where k_B is Boltzmann's constant and T is the temperature. Therefore, thermally driven errors are expected to be exceptionally rare. Figure 5(c) confirms this, extrapolating the histograms for these bit values to predict that it would take a349σ event for the "0" state to be mistaken for a "1" or a 47σ event for the reverse to occur. Thus, statistical errors in logical operations using our nanomechanical computing architecture can be safely ignored, with errors

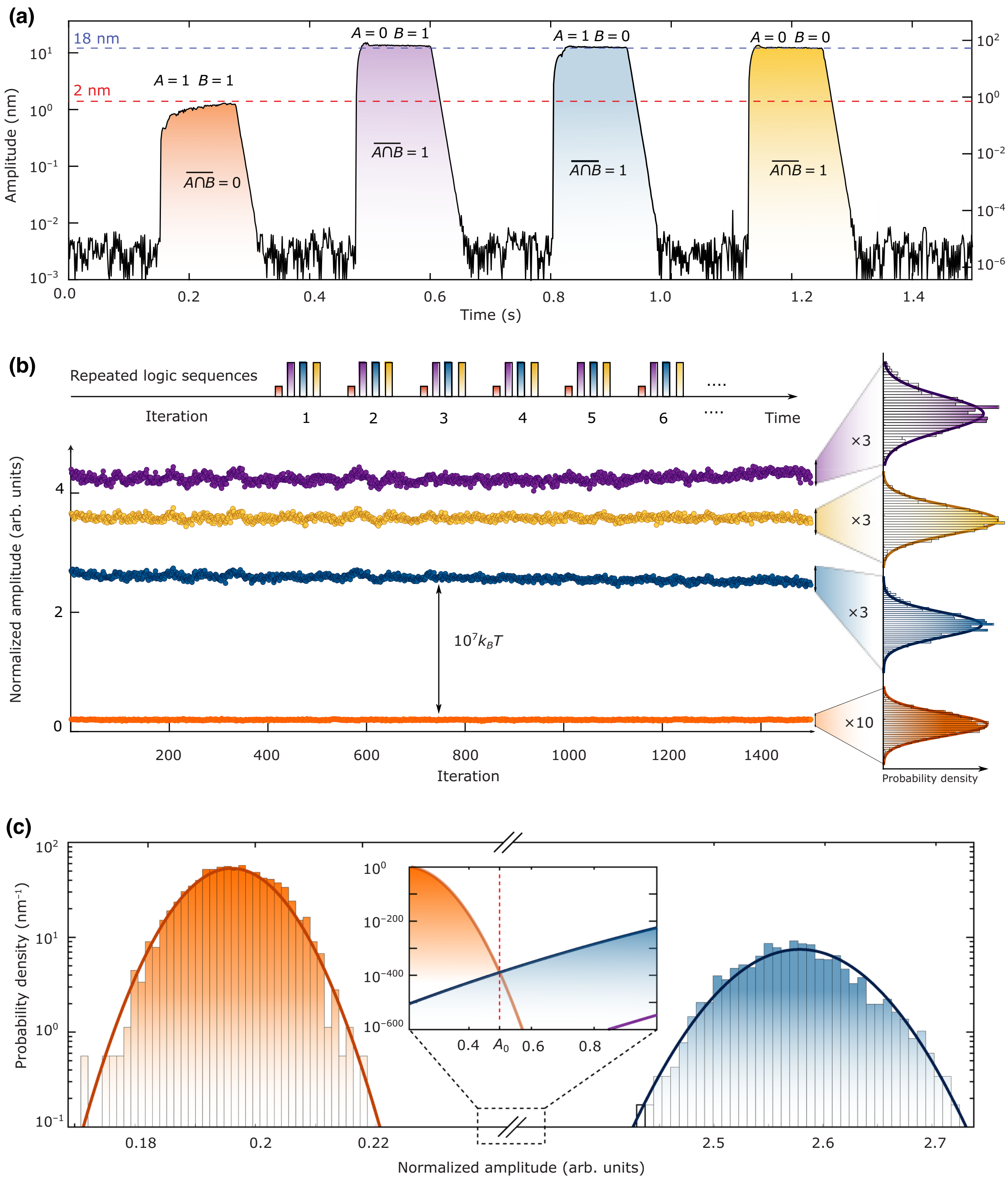

FIG. 5. NAND-gate truth table. (a) Time trace showing the measured resonator amplitude for all four combinations of logical inputs when our nanomechanical device is configured to implement a universal NAND gate. This time trace was acquired on a spectrum analyzer centered at the drive frequency Ω, operated in “zero-span” mode, with a resolution bandwidth of 510 Hz. This corresponds to a single acquisition without averaging. (b) Time evolution of the amplitudes of each of the four NAND-gate outputs over 1500 measurements, corrected for slow time drift due to chip heating effects (see Appendix I). Histograms are plotted on the right. These are found to be consistent with Gaussian distributions (solid lines), as expected from the central-limit theorem. The range of amplitudes for a logical “0” state is significantly smaller than that for “1” states, consistent with its smaller absolute amplitude of oscillation. (c) Histograms of the output-bit amplitudes for “11” and “10” inputs. The inset shows an interpolation of the histogram fits, illustrating the low probability of a statistical error. All results were obtained with a drive-resonator detuning of approximately 660 Hz.

likely dominated in practice by external perturbations to the system.

V. DISCUSSION

We have experimentally shown that the nonlinear Duffing bistability can be used to perform a universal set of logic operations, that these operations can be driven mechanically through on-chip acoustic waveguides and at a single frequency of operation, and that efficient coupling can be achieved between waveguides and gates. The coupling efficiency approaches unity, compared with 1 part in-10^7 efficiencies reported in previous approaches with electrical interconnects [19].

The acoustically driven single-frequency nanomechanical logic gate reported here addresses some barriers to the realization of scalable mechanical computing. However, substantial challenges remain, including the reproducibility of fabrication from gate to gate, miniaturization from microscale to nanoscale, acoustic phase synchronization, and understanding and control of the interactions between large networks of nonlinear resonators. Scale-up will likely require new fabrication approaches and developments, modeling and potentially mitigation of the interactions between resonators, and precise engineering of both acoustic paths and electrical phases, and may also require analog electrical control.

The $10^7 k_B T$ energy cost of our logic operations is far above the Landauer limit since, to transition between states, the mechanical resonator must be driven above its critical energy (28 fJ $\sim 7 \times 10^6 k_B T$).

This leads to a relatively high single-gate power consumption of 0.98 pW (see Appendix G). Because of the long mechanical decay time of our gates, our demonstration is also slow, with each gate operation lasting at least 10 ms. Speed could be increased and critical energy lowered, both through miniaturization and material engineering. For instance, graphene nanomechanical resonators have been demonstrated with a size as small as 500 nm [42] and resonance frequencies in the gigahertz regime [43,44]. We show in Appendix K that use of a low-quality graphene resonator ($Q \sim 60$) with these properties could enable an energy cost approaching the Landauer limit and gate speeds above 100 MHz.

ACKNOWLEDGMENTS

This research was primarily funded by the Australian Research Council and the Lockheed Martin Corporation through Australian Research Council Linkage Grant No. LP190101159. Support was also provided by the Australian Research Council Centre of Excellence for Engineered Quantum Systems (Grant No. CE170100009). This work was performed in part at the Queensland node of the Australian National Fabrication Facility and the Australian Microscopy & Microanalysis Research Facility at the Australian Centre for Microscopy and Microanalysis. G.I.H. and C.G.B. acknowledge the Australian Research Council (Grants No. DE210100848 and No. DE190100318, respectively). The authors acknowledge HCPhotonics for providing a second-harmonic module that was used in the heterodyne probing system.

APPENDIX A: FABRICATION DETAILS

The devices are fabricated on a chip that is diced from a commercially available wafer that has a film of stoichiometric silicon nitride (Si_3N_4) deposited on a silicon substrate. The Si_3N_4 film is approximately 80 nm thick with a tensile stress σ of 1 GPa. We pattern the electrodes through a combination of electron-beam lithography and evaporation of gold (approximately 50 nm), followed by lift-off. The hole pattern in the Si_3N_4 film is created by electron-beam lithography and reactive-ion etching. This pattern consists of a grid of 1-μm-square holes separated by 2 μm (center to center). The Si_3N_4 membrane is then released from the silicon substrate via a potassium hydroxide wet etch; at this point, the structured mesh has an effective stress σ_T of 0.67 GPa [35]. On each chip we define arrays of devices, each consisting of an 80-μm-square mechanical resonator connected with tunnel barriers to single-mode input and output acoustic waveguides.

To avoid reflections and resonances between the three gold on-chip electrodes, the acoustic impedance between the silicon nitride waveguide without gold and the silicon nitride waveguide with gold needs to be matched. This is done by our patterning nine gold pads on the waveguide between the on-chip electrodes, minimizing the impedance difference. Similarly, to efficiently launch the acoustic wave in the membrane, adiabatic tapering of the impedance is used with ten decreasing-size gold pads patterned on the left and right sides of electrodes A and P (see Fig. 2).

APPENDIX B: DERIVATION OF LINEAR AND NONLINEAR SPRING COEFFICIENTS

The nonlinearity present in our system is geometric [45] with nonlinear coefficient α. This nonlinearity emerges from a high-amplitude displacement of the mechanical resonator. α can be directly calculated from the mode shape and displacement of our resonators. Here we derive α for the simplest system, a 1D string, extend the derivation for a 2D membrane using numerical simulations, and finally derive it for a meshed membrane just as the one in our experiment.

1. String

The simplest system to consider is a 1D string, with undeflected length

$$L = \int_0^L dx, \tag{B1}$$

while the length L' of the deformed string is given by

$$L' = \int_0^L (\Delta x^2 + \Delta u^2)^{1/2} = \int_0^L \left(1 + \left(\frac{\partial u}{\partial x}\right)^2\right)^{1/2} dx. \tag{B2}$$

In a deflected string, the local change in string length is

$$dx\left(1 + \left(\frac{\partial u}{\partial x}\right)^2\right)^{1/2} - dx \sim \frac{1}{2}\left(\frac{\partial u}{\partial x}\right)^2 dx, \tag{B3}$$

which corresponds to a local strain

$$\varepsilon(x) = \frac{1}{2}\left(\frac{\partial u}{\partial x}\right)^2. \tag{B4}$$

The energy density $e(x)$ associated with this elongation is given by

$$e(x) = \frac{1}{2} YA\varepsilon^2 = \frac{1}{8} AY\left(\frac{\partial u}{\partial x}\right)^4, \tag{B5}$$

where A is the cross-section area of the string and Y the Young's modulus of the material. The total elongation energy is thus given by the integral over the volume:

$$E_{\text{elongation}} = \int_0^L e(x)dx = \frac{1}{8} YA \int_0^L \left(\frac{\partial u}{\partial x}\right)^4 dx. \tag{B6}$$

Identifying this with a quartic Duffing potential energy of the form $E = \frac{1}{4}\alpha x^4$, we get the nonlinear coefficient α:

$$\alpha = \frac{1}{2} YA \int_0^L \left(\frac{\partial u_0}{\partial x}\right)^4 dx, \tag{B7}$$

where u_0 is the unperturbed normalized displacement profile, normalized such that $\max(u_0) = 1$.

Similarly, since the energy stored in the string's kinetic energy in the form of tension is given by

$$E = \frac{1}{2}\rho A \int_0^L \left(\frac{\partial u}{\partial t}\right)^2 dx = \frac{1}{2}\sigma A \int_0^L \left(\frac{\partial u}{\partial x}\right)^2 dx \tag{B8}$$

we can identify the linear spring constant k and the effective mass $m_{\text{eff}} = k/\Omega^2$,

$$k = \rho\Omega_m^2 A \int u_0^2(x)dx = \sigma A \int_0^L \left(\frac{\partial u_0}{\partial x}\right)^2 dx \tag{B9}$$

and

$$m_{\text{eff}} = \rho A \int u_0^2(x)dx, \tag{B10}$$

both in geometric terms.

2. Membrane

For the 2D case, in the regime where the resonator is thin (i.e., the resonator is thin enough to behave as a membrane and not as a plate), the bending stiffness is ignored, and the Young's modulus is assumed to be isotropic. The membrane's Duffing nonlinear coefficient α, by analogy to the string case [Eq. (B7)], takes the form

$$\alpha = \frac{1}{2} Yh \iint \left(\left(\frac{\partial u_0}{\partial x}\right)^4 + \left(\frac{\partial u_0}{\partial y}\right)^4\right) dxdy, \tag{B11}$$

where h is the membrane thickness. Similarly, the spring constant k and effective mass $m_{\text{eff}} = k/\Omega_m^2$ take the forms

$$k = \sigma h \iint \left(\left(\frac{\partial u_0}{\partial x}\right)^2 + \left(\frac{\partial u_0}{\partial y}\right)^2\right) dxdy \tag{B12}$$

and

$$m_{\text{eff}} = \rho h \iint u_0^2(x,y)dxdy \tag{B13}$$

expressed in geometric terms.

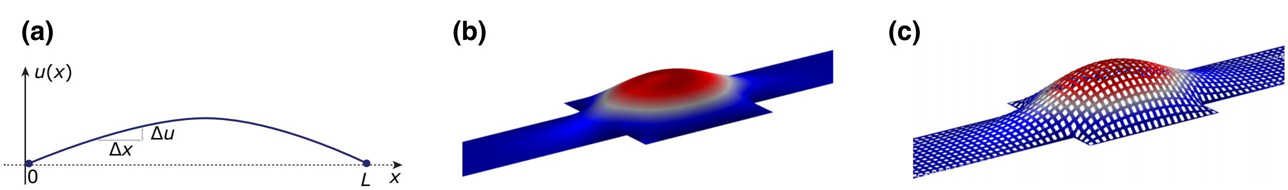

FIG. 6. Nanomechanical Fabry-Perot cavity. (a) Elongation energy in a deformed string. (b) FEM simulation of a nonmeshed acoustic Fabry-Perot cavity. Estimated parameters are as follows: $k = 418$ N/m, $m_{\text{eff}} = 5.11 \times 10^{-13}$ kg, $\alpha = 3.65 \times 10^{13}$ N/m^3, $x_{\text{crit}} = 16.5$ nm, and $\Omega_m = 4.5$ MHz. (c) FEM simulation of a meshed acoustic Fabry-Perot cavity. The estimated parameters are as follows: $k = 253$ N/m, $m_{\text{eff}} = 3.8 \times 10^{-13}$ kg, $\alpha = 2.64 \times 10^{13}$ N/m^3, $x_{\text{crit}} = 15$ nm, and $\Omega_m = 4.1$ MHz. The physical parameters are as follows: $Y = 250$ GPa, $\sigma = 1$ GPa, $\rho = 3100$ kg/m^3, and $Q = 28\,000$. The resonator width and length are 80 μm and the tunnel width is 44 μm.

Using the derived geometric terms, we can directly feed them into finite-element models (FEMs) such as in COMSOL MULTIPHYSICS. The numerical results are calculated for simple systems such as strings or membranes and are compared with the analytical expressions. Once verified, we modify the geometry and introduce the meshed membrane. The mode shapes obtained are plotted in Figs. 6(b) and 6(c). The boundary conditions are fixed all along the perimeter of the waveguide, tunnel, and resonator; the membrane is free to move only where it has been released, i.e., where the underlying silicon has been etched away. As is visible in the simulation, the resonator mode shape (which would have a sinusoidal displacement profile in a square resonator) is slightly modified by the presence of the tunnel junctions: the motion extends with exponentially decaying amplitude within the tunnel junctions as expected. From these simulations, we can extract the nonlinear coefficient for the meshed membrane $\alpha = 2.64 \times 10^{13}$ N/m^3.

APPENDIX C: ELECTROSTATIC ACTUATION AND ELECTRIC POWER REQUIREMENTS

In this section, we discuss the parameters of the electrostatic actuation required to generate the acoustic wave. Furthermore, we discuss the overall efficiency, electric plus acoustic. Acoustic energy requirements are discussed in Appendixes E and F.

A finite-element simulation of the electrostatic actuation process is shown in Fig. 7. It shows a cross section of the 500-μm-thick silicon wafer, covered by the 80-nm-thick silicon nitride membrane and a 40-μm-wide gold electrode. As these are approximately 10 000 times thinner than the wafer, they are visible only in the enlarged subplots. Actuation of the membrane is provided by the electrostatic interaction between the gold electrode atop the phononic waveguide and an electrode on the underside of the wafer (see also Figs. 2 and 3). The silicon handle wafer is p doped (boron), with a resistivity of 1–10 Ω cm. Therefore, its low-frequency permittivity ε is greatly enhanced over its optical frequency permittivity ($\varepsilon_{\mathrm{Si,THz}} = n^2 = 3.5^2 \sim 12$), due to charge transfer through the silicon, with a megahertz-range permittivity of approximately 10^4 (so-called colossal permittivity [46,47]). The effect of this is shown in Fig. 7, which plots the electric field in response to a 1-V bias applied between both electrodes. Because of the extremely large permittivity of doped silicon at megahertz frequencies, the electric energy density is well localized in the undercut region between the silicon nitride and the silicon substrate [see Fig. 7(c)]. This means the capacitance can be well approximated by that of a parallel-plate capacitor with an air gap ($C = \varepsilon_0 A/d$), with a plate separation d equal to the depth of the undercut. The error from this approximation is under 4% here, with a simulated capacitance per unit length (along the y direction) of 367 pF/m from the finite-element simulation and 354 pF/m from the parallel-plate approximation.

It is instructive to relate the mechanical energy stored in the membrane deflection to the stored energy in the capacitor. As justified above, we use the parallel-plate

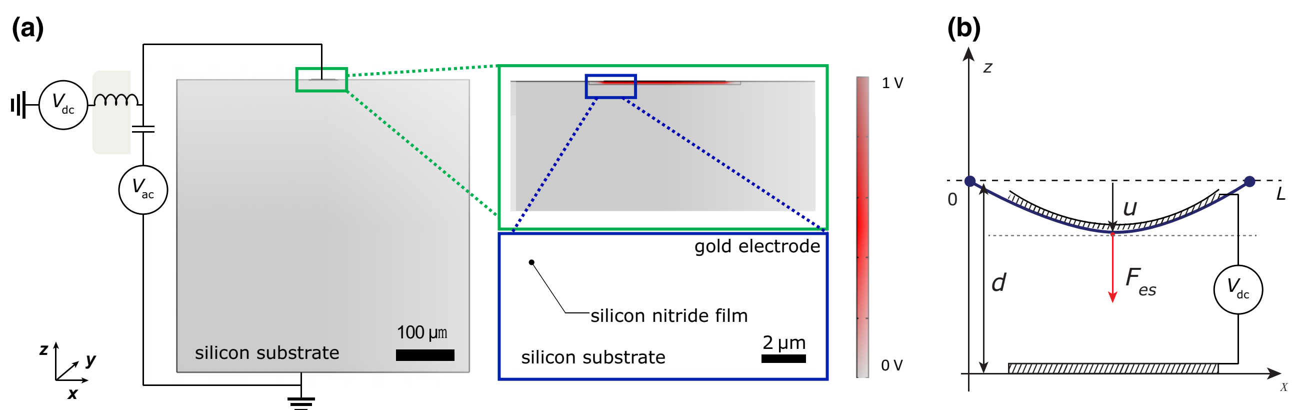

FIG. 7. (a) Two-dimensional electrostatic simulation of the electric potential in response to a 1-V dc bias applied between a gold electrode located above the released silicon nitride film and a ground plane below the silicon substrate. Because of the extremely high permittivity of doped silicon at megahertz frequencies, the electric energy density is well localized in the undercut region between the silicon nitride and the silicon substrate. This means the capacitance can be well approximated by that of a parallel-plate capacitor ($C = \varepsilon_0 \varepsilon_r A/d$) with a plate separation d equal to the depth of the undercut—with an error less than 4% here. The simulation parameters are as follows: substrate thickness 500 μm, undercut depth 1 μm, silicon permittivity 1×10^4, electrode width 40 μm, simulated capacitance per unit length 367 pF/m, and parallel-plate-approximation capacitance per unit length 354 pF/m. (b) Schematic showing the relevant parameters for the estimation of stored mechanical and electrostatic energies.

approximation. The mechanical energy stored in the deflection of amplitude u is given by

$$E_M = \frac{1}{2}ku^2 = \frac{1}{2}k\left(\frac{F_e}{k}\right)^2 = \frac{1}{2}\frac{F_e^2}{k}, \tag{C1}$$

where $F_e = \frac{1}{2}(\varepsilon_0 A/d^2)V^2$ is the electrostatic force applied on the membrane, in the limit of small displacements $u \ll d$. Similarly, the stored electrostatic energy in the capacitor is given by

$$E_e = \frac{1}{2}CV^2 = \frac{1}{2}\frac{\varepsilon_0 A}{d}V^2 = F_e d. \tag{C2}$$

The ratio η of these two energies, valid in the limit of small displacements, takes the form

$$\eta = \frac{E_M}{E_e} = \frac{F_e}{2kd} = \frac{\varepsilon_0 A V^2}{4kd^3} = \frac{1}{2}\frac{u}{d}. \tag{C3}$$

Note that this energy analysis can be readily converted to a power analysis when the waveguide is operated sufficiently high above its cutoff frequency, such that the group velocity of the acoustic wave is close to its phase velocity, $v_g \sim v_p \sim \sqrt{\sigma/\rho}$, in which case the acoustic energy has left the capacitor region before the start of a new cycle. In the current experiments, where the capacitor is charged with an ac voltage source, there is no fundamental lower bound on power loss in the electric circuit (Ohmic losses may, in principle, be made arbitrarily small). On the other hand, if the capacitive actuation is operated in a regime where a given fraction of the capacitor energy is lost during the charge-and-discharge process—as when the capacitor is charged from a constant-voltage power supply, which is the case for CPUs, where this fraction reaches 0.5 [41]—it is beneficial to operate in a regime of small capacitor gap d, which maximizes the electrostatic force for a given capacitor energy; see Eq. (C2). With use of an oxide sacrificial layer under the nitride as reported in Ref. [48], this gap can reliably be made sub-100 nm.

APPENDIX D: MEASUREMENT SETUP AND PHOTOCURRENT DERIVATION

We use here a laser vibrometer, as this allows us to read out the displacement amplitude at various positions along the waveguide or the resonator in a noncontact fashion [32,49]. This approach further allows direct imaging of the performance of the phononic circuits, for instance, through surface scans of acoustic wave propagation and tunneling [35,50]. For further integration, this optical readout can be converted to electrical readout of the output of the phononic circuit, as has been demonstrated on a variety of nanomechanical platforms [51], including 2D membranes under tensile stress [52,53].

In this measuring system, the optical probe field E_p is reflected off the oscillating membrane (Fig. 3). For a given polarization, the probe field can be expressed as

$$E_p = A_p \exp(i\omega t + \phi), \tag{D1}$$

where A_p is the amplitude of the field, Ω is its frequency, and ϕ is the phase modulation created by the change of the light-path length due to the membrane motion. Here, for simplicity, we have ignored any noise in amplitude and phase of the field and we have chosen a fixed observation position at the position of the detector. Similarly, the local-oscillator field E_{LO} can be expressed as

$$E_{\mathrm{LO}} = A_{\mathrm{LO}} \exp\left[i(\omega + \omega_{\mathrm{AOM}})t\right] \tag{D2}$$

where A_{LO} is the amplitude of the field and ω_{AOM} is the frequency shift created by the acousto-optical modulator (AOM). These two fields interfere, and once detected, the photocurrent i transduced by the detector is given by

$$i \propto A_p^2 + A_{\mathrm{LO}}^2 + 2A_p A_{\mathrm{LO}} \cos(\omega_{\mathrm{AOM}} t - \phi). \tag{D3}$$

Since the membrane is driven with a sinusoidal excitation at frequency ω, ϕ can be expressed as $\phi = A_\phi \cos(\Omega t)$, with A_ϕ the amplitude of the phase modulation in radians. With use of the Jacobi-Anger relation, to first order, the response of the detector at frequencies $\omega_{\mathrm{AOM}} \pm \Omega$ is $i(\omega_{\mathrm{AOM}} \pm \Omega) \propto [\sin(\omega_{\mathrm{AOM}} - \Omega)t) - \sin((\omega_{\mathrm{AOM}} + \Omega_m)t)]$, where the amplitude of the photocurrent at frequencies $\omega_{\mathrm{AOM}} \pm \Omega$ is proportional to the amplitude of the membrane motion. Meanwhile, the photocurrent at frequency ω_{AOM} is given by

$$i(\omega_{\mathrm{AOM}}) \propto A_p A_{\mathrm{LO}} \cos(\omega_{\mathrm{AOM}} t). \tag{D4}$$

Furthermore, to first order, $i(\omega_{\mathrm{AOM}} \pm \Omega)/i(\omega_{\mathrm{AOM}}) = A_\phi/2$. Knowing that $A_\phi = 2\pi$ corresponds to 780 nm, the free-space wavelength of the laser, we can directly retrieve the amplitude of motion of the membrane in nanometers. Typically, in our experiment, when the membrane is driven to high amplitude, the amplitude of the photocurrent at ω_{AOM} and at $\omega_{\mathrm{AOM}} \pm \Omega$ is 0.14 $\mathrm{V_{rms}}$ (−4 dBm) and 0.022 $\mathrm{V_{rms}}$ (−20 dBm), respectively, which give an amplitude of motion of approximately 19 nm.

APPENDIX E: CRITICAL AMPLITUDE AND CRITICAL ENERGY

The total energy E of the resonator is given by

$$E = \frac{1}{2}kx^2 + \frac{1}{4}\alpha x^4 = \frac{1}{2}m_{\mathrm{eff}}\Omega_m^2\left(1 + \frac{\alpha}{2k}x^2\right)x^2, \tag{E1}$$

where the resonance frequency is amplitude dependent:

$$\Omega = \Omega_m\left(1 + \frac{\alpha}{2k}x^2\right)^{\frac{1}{2}}. \tag{E2}$$

The frequency shift $\delta\Omega(x)$ is given by

$$\delta\Omega(x) = \frac{\alpha}{4k}\Omega_m x^2, \tag{E3}$$

where α is the nonlinear coefficient. The critical amplitude is reached when this amplitude-dependent frequency shift $\delta\Omega \sim \Gamma = \Omega_m/Q$, that is,

$$x_{\mathrm{crit}} = \sqrt{\frac{2k\Gamma}{3\alpha\Omega_m}} = \sqrt{\frac{2\Gamma\Omega_m m_{\mathrm{eff}}}{3\alpha}} = \sqrt{\frac{2k}{3\alpha Q}}. \tag{E4}$$

Using these derivations, we calculate the linear elongation energy for a string [Fig. 6(a)], for an evanescently coupled membrane [Fig. 6(b)] and for an evanescently coupled meshed membrane [Fig. 6(c)]. The meshed case has lower mass and frequency compared with the unperturbed membrane. The critical amplitude is, however, not significantly reduced, since both k and α drop by comparable amounts (divided by 1.65 vs 1.4). This observation is expected, as the mode profile is essentially unperturbed by the subwavelength hole pattern.

Finally, the last relevant parameter is the critical energy E_{crit}, which is the energy cost associated with taking the resonator amplitude to the critical amplitude, defined as

$$E_{\mathrm{crit}} = \frac{1}{2}kx_{\mathrm{crit}}^2 = \frac{k^2}{3\alpha Q} = \frac{m_{\mathrm{eff}}^2\Omega_m^4}{3\alpha Q}. \tag{E5}$$

It is important to notice that most of the energy stored in the resonator corresponds to the linear elastic energy. Since $\frac{1}{2}kx^2 \gg \frac{1}{4}\alpha x^4$, the energy arguments presented in Eq. (F7) refer to the energy in the linear regime, but apply to the nonlinear case.

APPENDIX F: ENERGY-COST DERIVATION

In practice, the energy cost depends on other parameters, specifically the desired contrast between the "0" and "1" amplitudes, the duration of the logic pulses, and how much of the energy in the Duffing oscillator is transmitted into the output waveguide (and therefore not lost). We develop a simple model of the total energy cost, in the limit that the pulse duration is long compared with the decay time of the nanomechanical resonator and that most of the energy in the gate comes from the pump. The model predicts different energy costs and functional dependencies for "0" and "1" output states. This can be understood directly from the difference in amplitudes of the two outputs: to achieve a lower amplitude for a "0" the gate must reject more of the input energy. The results of the model are shown as a function of the level of impedance matching of the resonator in Fig. 4(d) with use of the calibrated Duffing coefficient and spring constant of our resonators.

To estimate the energy cost for a single operation in our device, we consider the double-sided nonlinear mechanical

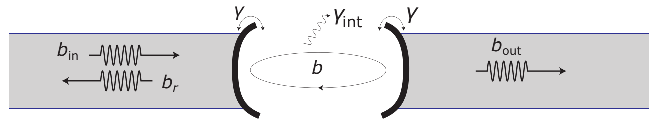

FIG. 8. Double-sided mechanical resonator. Schematic of the model used to calculate the energy cost of each logic operation. The double-sided mechanical resonator is excited by an input wave of amplitude x_{in} with coupling rate γ. The waves exiting the cavity on the right (x_{out}) and left (x_{r}) are also coupled out of the cavity at rate γ. γ_{int} is the intrinsic cavity loss rate.

cavity in Fig. 8, which oscillates with an amplitude proportional to $|b|$ with energy $E = |b|^2$, when excited by an input acoustic wave of power $|b_{\mathrm{in}}|^2$. The power of the wave exiting the right side of the cavity is $|b_{\mathrm{out}}|^2$ and the power of the wave reflected by the cavity is $|b_r|^2$. The equation of motion of such a cavity is given by [54]

$$\dot{b} = -\frac{\gamma_{\mathrm{tot}}}{2}b - i\Delta b + \sqrt{\gamma}b_{\mathrm{in}}, \tag{F1}$$

where $\gamma_{\mathrm{tot}} = 2\gamma + \gamma_{\mathrm{int}}$ is the total energy loss rate, γ is the coupling rate of both sides of the cavity, γ_{int} is the intrinsic loss rate of the cavity, Ω is the angular frequency of the exciting wave, and $\Delta = \Omega - \Omega_m$ is the drive-frequency detuning from the cavity resonance Ω_m. This equation can be solved for the steady state when the duration of the acoustic wave pulse $t = N/\gamma_{\mathrm{tot}}$ is longer than the inverse of the decay rate. This is the case here since the quality factor of the resonators is around 10^4, leading to a decay rate of hundreds of hertz, the inverse of which is 2 orders of magnitude smaller than the pulse duration used. In this situation, $N \gg 1$ and $\dot{b} \sim 0$, which leads to

$$b = \frac{\sqrt{\gamma}}{\gamma_{\mathrm{tot}}/2 + i\Delta}b_{\mathrm{in}}. \tag{F2}$$

As shown by Fig. 8, $b_{\mathrm{out}} = \sqrt{\gamma}b$; therefore, the steady-state efficiency defined as $\eta = |b_{\mathrm{out}}|^2/|b_{\mathrm{in}}|^2$ can be expressed as

$$\eta = \frac{\gamma^2}{\gamma_{\mathrm{tot}}^2/4 + \Delta^2}. \tag{F3}$$

With use of Eq. (F2), the mechanical energy E of the cavity is then given by

$$E = \frac{\gamma}{\gamma_{\mathrm{tot}}^2/4 + \Delta^2}|b_{\mathrm{in}}|^2. \tag{F4}$$

The steady-state energy can be expressed as a fraction A of the critical energy E_{crit}, $E = AE_{\mathrm{crit}}$, where $A = A^{(1)} > 1$ when the Duffing oscillator is in the high-amplitude state, corresponding to a logic operation output "1," and $A = A^{(0)} < 1$ when the oscillator is in the low-amplitude state, corresponding to a logic operation output “0.” Therefore, we have

$$|b_{\rm in}|^2 = \frac{AE_{\rm crit}(\gamma_{\rm tot}^2/4 + \Delta^2)}{\gamma}. \tag{F5}$$

Since the right output of the cavity guides the result of the logic operation, only the wave propagating away from the cavity in the left direction and the energy lost to the environment at rate $\gamma_{\rm int}$ will contribute to the losses (Fig. 8). Therefore, the energy lost $E_{\rm lost}$ during the logic operation can be expressed as [54]

$$E_{\rm lost} = \int_0^T (|b_{\rm in}|^2 - |b_{\rm out}|^2)dt. \tag{F6}$$

Given $b_{\rm out} = \sqrt{\gamma}b$ and, for the steady state, $b_{\rm in}$ can be assumed to be constant as a function of time. Therefore, using Eqs. (F2) and (F5), we have

$$E_{\rm lost} = \frac{NAE_{\rm crit}}{\gamma_{\rm tot}\gamma}\left(\frac{\gamma_{\rm tot}^2}{4} + \Delta^2 - \gamma^2\right). \tag{F7}$$

When the output of the logic operation is a binary “1,” $A = A^{(1)} > 1$ and $\Delta = \Delta^{(1)} = 0$ since the cavity has shifted on resonance. With use of Eq. (F7), the energy lost for an output “1” [output 1 in Fig. 4(d)], $E_{\rm lost}^{(1)}$, is therefore given by

$$E_{\rm lost}^{(1)} = \frac{NA^{(1)}E_{\rm crit}}{4}\left(\frac{\gamma_{\rm int}}{\gamma}\right)\left(2 - \frac{\gamma_{\rm int}}{\gamma_{\rm tot}}\right), \tag{F8}$$

where we have used the relation $\gamma_{\rm tot} = 2\gamma + \gamma_{\rm int}$.

When the output of the logic is a binary “0,” $A = A^{(0)} < 1$. However, the detuning is not negligible since the resonance frequency of the Duffing oscillator has not shifted to the driving frequency. Because the acoustic pump signal excites the oscillator close to the critical energy independently if the logic operation result is a “0” or a “1,” the contribution of the acoustic signal A and B to the input acoustic power will be negligible and we can assume that $b_{\rm in}^{(1)} \sim b_{\rm in}^{(0)}$. The detuning can then be expressed with use of Eq. (F5) as

$$\Delta^{(0)} = \sqrt{\frac{\gamma_{\rm tot}^2}{4}\left(\frac{A^{(1)}}{A^{(0)}} - 1\right)}. \tag{F9}$$

With use of Eq. (F7), it is straightforward to see that the energy lost when the output of the logic operation is a “0” [output 0 in Fig. 4(d)] is given as follows:

$$E_{\rm lost}^{(0)} = \frac{NA^{(1)}E_{\rm crit}}{4}\left(\frac{\gamma_{\rm tot}}{\gamma} - \frac{4\gamma}{\gamma_{\rm tot}}\left(\frac{A^{(0)}}{A^{(1)}}\right)\right). \tag{F10}$$

The evolution of $E_{\rm lost}^{(0)}$ and $E_{\rm lost}^{(1)}$ as a function of $Q/Q_{\rm int} = \gamma_{\rm int}/\gamma_{\rm tot}$ is displayed in Fig. 4(d). For Fig. 4(d), we use the experimental values of Ω_m, $\gamma_{\rm int}$, γ, and N. $m_{\rm eff}$ and α are calculated from finite-element simulation using the equations in Appendix B.

As can be seen, the energy cost for an output “1” state increases monotonically as the resonator becomes increasingly undercoupled, while it goes to a constant minimum value expressed as $E_{\rm lost,min}^{(1)} = NAE_{\rm crit}(\gamma_{\rm int}/\gamma_{\rm tot})$ in the impedance-matched regime, where the loaded Q is much smaller than $Q_{\rm int}$. By contrast, the energy cost for an output “0” state is optimal when $Q/Q_{\rm int} = 0.49$, in between the well-impedance-matched and poorly-impedance-matched regimes. The increased energy cost at low Q in this case can be understood because as Q decreases, the decay rate of the resonator increases, so a larger nonlinear frequency shift is required to operate the gate. Achieving this larger shift requires a higher amplitude of drive, and therefore increases the energy cost.

TABLE I. Values of the energies involved in the gate operation considering $Q = 28\,000$.

Parameter	Energy (fJ) (gate 10 ms)	Energy (fJ) (gate 120 ms)	Expression
Energy lost (0)	33	400	$E_{\rm lost}^{(0)} = \frac{NA^{(1)}E_{\rm crit}}{4}\left(\frac{\gamma_{\rm tot}}{\gamma} - \frac{4\gamma}{\gamma_{\rm tot}}\left(\frac{A^{(0)}}{A^{(1)}}\right)\right)$
Energy lost (1)	7	77	$E_{\rm lost}^{(1)} = \frac{NA^{(1)}E_{\rm crit}}{4}\left(\frac{\gamma_{\rm int}}{\gamma}\right)\left(2 - \frac{\gamma_{\rm int}}{\gamma_{\rm tot}}\right)$
Critical energy	28	28	$E_{\rm crit} = \frac{1}{2}kx_{\rm crit}^2 = \frac{k^2}{3\alpha Q} = \frac{{m_{\rm eff}}^2\Omega_m^4}{3\alpha Q}$
Average energy cost	20	240	$\bar{E} = \frac{1}{2}\left(E_{\rm lost}^{(1)} + E_{\rm lost}^{(0)}\right)$
Minimum average energy cost	10	124	$0 = \frac{d\bar{E}(Q)}{dQ}$

Our experiments are performed in the near-impedance-matched regime, with $\gamma_{\text{int}}/\gamma \sim 0.2$, $\gamma_{\text{int}}/\gamma_{\text{tot}} \sim 0.1$, and $\gamma_{\text{tot}}/\gamma \sim 2$. The measured oscillation amplitudes of 2 and 18 nm, respectively, for a "0" and a "1" give a ratio $A^{(0)}/A^{(1)} = (2/18)^2 \sim 0.01$. The oscillation energy of a "1" is around 40% higher than the critical energy, with $A^{(1)} = (x^{(1)}/x_{\text{crit}})^2 = (18\text{ nm}/15\text{ nm})^2 = 1.4$. For the data shown in Sec. IV, $N \sim 18$, while for our shorter, 10-ms-duration gates, this reduces to $N \sim 1.5$. Using these parameters in Eqs. (F10) and (F8), we find that the energy lost during an operation of our longer gates is roughly $2.7E_{\text{crit}}$ and $14E_{\text{crit}}$ for an output "1" and an output "0," respectively, while the equivalent energy losses for our shorter gates are roughly $0.21E_{\text{crit}}$ and $1.1E_{\text{crit}}$, respectively. Assuming an even distribution of operations resulting in "1" or "0," the average energy consumption is 240 and 20 fJ for our longer gates and shorter gates, respectively.

Previously reported microelectromechanical and nanoelectromechanical systems have been shown to perform logic operations with lower energy cost. For example, Ref. [27] shows logic operations using only 2 fJ of energy ($8 \times 10^5 k_B T$), Ref. [19] shows logic operations using only 0.1 fJ ($2 \times 10^4 k_B T$) and Ref. [10] shows logic operations using only 0.1 fJ ($2 \times 10^4 k_B T$) [55]. Even with this lower energy cost, however, cascading of these devices is challenging, both because, for some platforms, such as the one presented in Ref. [27], the output and input signals have different frequencies and because they rely on coupling of acoustic degrees of freedom to other degrees of freedom—typically electrical. Poor impedance matching between acoustic and electrical degrees of freedom significantly increases the total energy cost. For instance, when acoustic impedance mismatch is considered in the energy-cost calculation in Ref. [19], the energy cost per operation reaches $10^9 k_B T$ [19]. The direct coupling to and from acoustic waveguides that we demonstrate resolves this problem.

The peak power consumption P_{peak} of our logic gate is given by

$$P_{\text{peak}} = \frac{E_{\text{lost}}^{(0)} + E_{\text{lost}}^{(1)}}{2t}, \tag{F11}$$

where t is, again, the logic pulse duration, and the time-average power consumption P_{av} is given by

$$P_{\text{av}} = \frac{P_{\text{peak}} t}{\tau} = \frac{E_{\text{lost}}^{(0)} + E_{\text{lost}}^{(1)}}{2\tau}, \tag{F12}$$

where τ is the time between logic operations (or the inverse clock rate). For τ equal to twice the pulse duration, so the gate spends equal lengths of time ON and OFF, we find, using Eq. (F12), that the average power consumption is around 980 fW.

The main weakness of resonator-based logic is that when resonators are excited, they lose energy, even when they are not performing logic operations. This effect is reduced in our architecture. The energy that leaves the resonator goes into the output acoustic waveguide rather than as loss into the environment. A small circuit of 100 000 gates, capable of, for example, operating as a basic servo controller, would then expend 98 μW. This power loss can be reduced by sequentially clocking each column of gates on only at times when the information flow reaches them and for the period of a gate operation.

The power loss can be further reduced via miniaturization, as discussed in Appendix J. Taking the parameters of a 100-nm graphene drum detailed in Appendix J, we estimate an energy cost per operation of 63 zJ ($15k_B T$), assuming the same ratio of amplitudes ($A^{(0)}/A^{(1)}$), the same ratio of energy loss rates (γ_{int}, γ, and γ_{tot}), and the same number of periods in a logic pulse ($N = 18$). Supposing that each resonator is excited only 10% of the time ($\tau = 10t$), a circuit of 10^9 such gates would lose 6.3 pJ per cycle compared with 100 nJ for an equivalent CMOS circuit with 10^9 transistors (7-nm node) that each consume 1 fJ per operation [56].

APPENDIX G: OTHER LOGIC GATES

1. XOR gate

The first attempts to perform gate operations required us to overlap the signals A and B on the basis of delays between them. One of the first gates that we demonstrated was the XOR gate, shown in Fig. 9. To demonstrate the XOR gate, the pump P is not required. Here we measured optically the mechanical motion for A and B independently. Then we overlapped the two acoustic signals and read out optically the XOR value shown in black. Our experiments improved and we developed an interface to trigger each signal independently, including the pump P, allowing us to perform a universal gate such as the NAND gate shown in Fig. 5.

2. AND and OR gates

AND and OR gates are not demonstrated experimentally because they can be implemented with two and three NAND gates, respectively. However, our architecture can easily be adapted to perform AND and OR gates by initialization of the system in the "0" state. This can be achieved by one slightly reducing the amplitude of the pump to almost reach the "1" state. The A and B inputs would therefore interfere constructively with the pump to make the resonator jump into the "1" state. For an AND gate, constructive interferences between P and both A and B will be needed to make the gate jump to the high-amplitude state, since A AND B is equal to "1" only if both A and B are equal to "1." For an OR gate, interference between P and either A

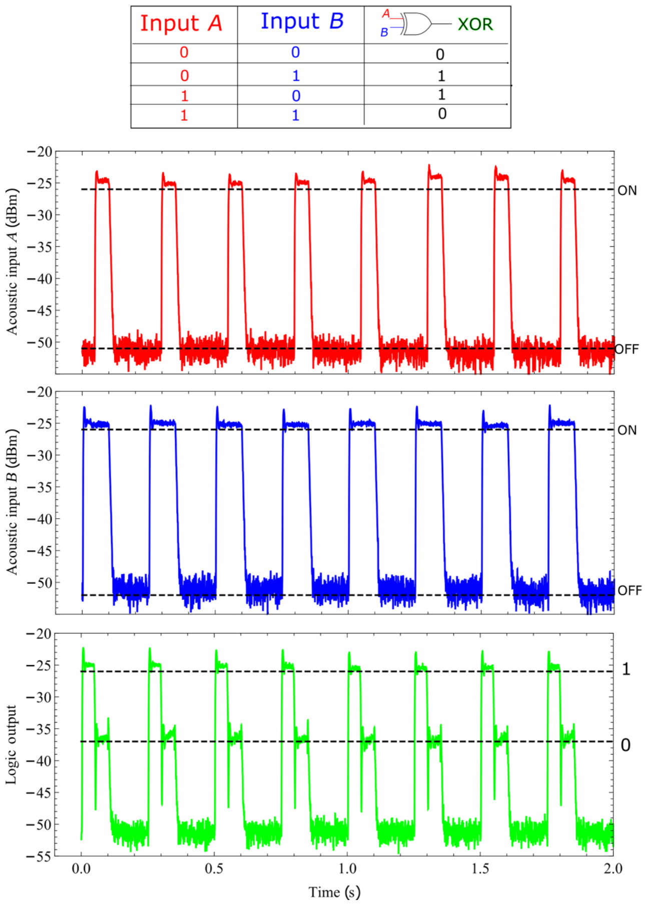

FIG. 9. XOR gate. Example of a repeated XOR gate using delay between A and B to form different overlaps that allow the four possible combinations of inputs per iteration.

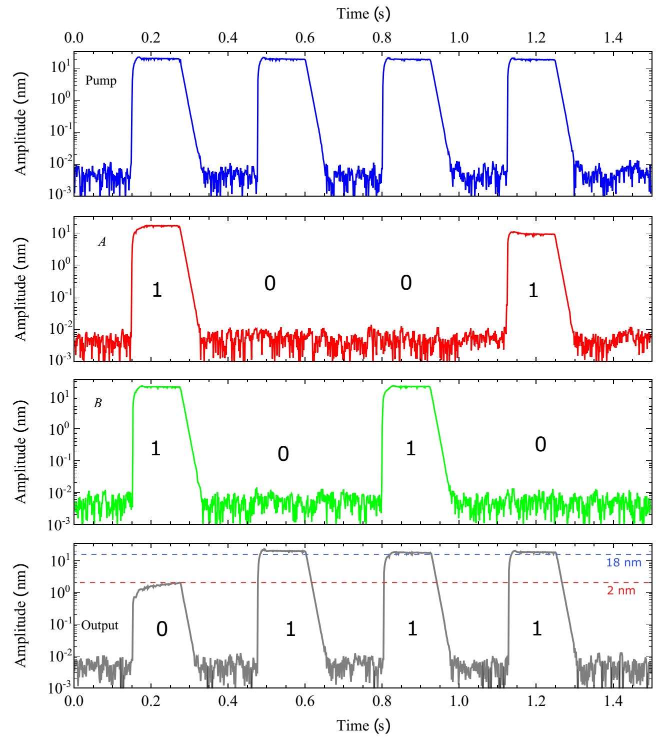

FIG. 10. Actuation protocol of individual acoustic inputs (pump, A, and B) to the NAND gate. Each input is the acoustic response driven by an electrical signal with a carrier frequency $2\pi\Omega$ and with an envelope of a 120-ms pulse and a delay of 200 ms between pulses.

or B should be enough to make the resonator jump since A OR B is equal to "1" if either A or B is equal to "1."

APPENDIX H: RELIABILITY AND FATIGUE

1. Nanomechanical gate sequence

To create the truth table sequence in Fig. 5(a), we use a series of transistor-transistor-logic pulses to trigger short bursts of coherent drive from three signal generators. The first of these three signal generators is used to create the electronic actuation for the pump, which consists of a sinusoidal wave at Ω gated by four 120-ms square pulses separated by 300 ms. The other two signal generators are used similarly to create the actuation for logical inputs A and B. The resonator's amplitude of oscillation due to these pulses is shown in Fig. 10. The phase of the three sinusoidal signals is adjusted to create a NAND gate as explained in Sec. IV. The transistor-transistor-logic pulses also trigger a spectrum analyzer to record the amplitude of motion of the membrane at the drive frequency Ω with zero span and a resolution bandwidth of 510 Hz. In Fig. 5(a) we show a sequence that demonstrates a NAND gate, where the pump and two logic inputs A and B have a carrier frequency Ω that is slightly blue detuned from the bare resonant frequency Ω_m (i.e., $\Omega > \Omega_m$). The ratio of the amplitudes of the "0" and "1" states is close to a factor of 10, due to the nonlinear mechanical response of the resonator [Fig. 4(c)].

2. Fatigue testing

To test for mechanical fatigue, we pumped a logic gate continuously for 2 months, corresponding to more than 10^{13} cycles, and separately performed around 10^6 logic operations. We observed no statistically significant changes in mechanical quality factor or nonlinearity in either experiment.

Similarly to what is observed for one of the devices (barrier length of 78 μm) in Fig. 4, due to manipulations and transport of the chip during the 2 months of the duration of the experiment, some devices were damaged. This is the reason why we performed our NAND-gate experiments with the device with a Q factor of 28 000 rather than the device with a Q factor close to the optimal energy consumption. It is important to note that these degradations were not due to fatigue but we due to environmental hazards that can easily be suppressed with proper chip protection.

3. Error-statistic setup

To record the data displayed in Figs. 5(b) and 5(c), the pulse sequence shown in Fig. 5(a) is repeated over 1500 times. However, for this measurement, we operate with a resolution bandwidth of 100 Hz and record only the central point of each pulse displayed on the spectrum analyzer.

APPENDIX I: DRIFT CORRECTION

Each point i of the four traces shown in Fig. 5(b) represents the mean value around the center (within the resolution bandwidth window) of each NAND gate. During the data acquisition of error statistics [Fig. 5(b)], a slow drift of the amplitude of each window was observed, due to thermal effects. The maximum drift was observed for the red trace, and dropped by 2.7 dBm after 0.6 h of continuous measurements. To remove this systematic error from our measurement, the drift was compensated by our applying the same simple linear transformation to the four traces. That is to say, each point i of the four traces is transformed $i \to i'$ as $i' = m \times i + p$. The blue trace (named A) and the red trace (named B) in Fig. 5(b) were used as a reference. We define the variables m and p as follows:

$$m = \frac{\overline{A} - p}{\langle A \rangle}, \quad p = \frac{\overline{B}\langle A \rangle - \overline{A}\langle B \rangle}{\langle A \rangle - \langle B \rangle}, \tag{I1}$$

where $\overline{X}$ represents the average of X over the 1500 measurements and $\langle X \rangle$ represents the moving average of X over a window of 100 measurements centered at point i but excluding point i. The resulting corrected data are presented in Fig. 5(b), which shows that the systematic error caused by drift is corrected efficiently. Histograms are plotted on the right in Fig. 5(b). These are found to be consistent with Gaussian distributions (solid lines), as expected from the central-limit theorem.

Temperature control at the level of the chip with Peltier elements and a proportional-integral-derivative feedback loop can be used to stabilize the temperature of the chip. In experiments built after the work reported in this paper, we installed such temperature control, and we observed a significant reduction of thermal drift, which entirely removed the need for drift corrections in postprocessing

1. Fabrication variability

Resonators fabricated with the same nominal parameters can exhibit variations in their mechanical properties, such as their resonance frequency and Duffing coefficient. When one is concatenating resonators to build a nanomechanical circuit, this may lead to challenges. This is particularly the case with high-Q, dissipation-diluted resonators, whose Q factors can reach 10^8. In our work, we use devices with lower Q factors (in the 10^4–10^5 range), which are therefore less sensitive to these effects, and we did not observe deviations in resonance frequency larger than the resonance linewidth in our experiments. Moreover, for higher operating bandwidth and faster logic operation, further reduction of the resonator quality factors is desirable, providing even better resonance frequency overlap. This reduction in Q factor is not due to energy loss in the material, but is due to a stronger acoustic coupling to the waveguides through the tunnel junctions. In the case where high Q factors are needed, to circumvent fabrication-induced variability, resonance frequencies of individual devices can alternatively be tuned by application of a dc voltage to an electrode situated on top of the resonator (as shown, for instance, in Ref. [57]). This method also allows precise synchronization of as many resonators as required and could be applied to tune and bring on resonance multiple resonators even in the case of very narrow linewidths. On the other hand, adjustment of the resonance frequency with dc voltage can also be used to detune devices from each other and prevent them from interacting with each other. This feature can be useful, for example, to prevent instabilities and limit cycle behavior, which are known to happen in systems as small as ones comprising two oscillators (see Refs. [58,59]). Such chaotic behavior could prevent the use of nanomechanical gates for computing and could be a serious challenge when the number of gates required is large.

APPENDIX J: SCALING WITH RESONATOR SIZE

Here we quantify how changing the resonator dimensions and material can increase its speed and reduce its energy consumption. We consider an out-of-plane flexural motion of a square membrane of side L, thickness h, density ρ, and Youngs's modulus Y under tensile stress σ. The mode profile u takes the form

$$u(x, y) = \sin\left(\frac{n\pi x}{L}\right) \sin\left(\frac{m\pi y}{L}\right). \tag{J1}$$

We consider hereafter the fundamental $n = 1$, $m = 1$ mode, with effective mass given by

$$m_{\text{eff}} = \frac{1}{4} L^2 h \rho, \tag{J2}$$

spring constant given by

$$k = \frac{1}{2}\pi^2 h\sigma, \tag{J3}$$

and nonlinear Duffing coefficient given by Eq. (B11) expressed as

$$\alpha = \frac{9\pi^4 hY}{64 L^2}. \tag{J4}$$

In the linear regime, the oscillation has a small amplitude, and the resonance frequency Ω_m is given by

$$\Omega_m = \sqrt{\frac{k}{m_{\mathrm{eff}}}} = \frac{\sqrt{2}\pi}{L}\sqrt{\frac{\sigma}{\rho}}, \tag{J5}$$

where we recognize the speed of sound $\sqrt{\sigma/\rho}$. The critical amplitude x_{crit} given by Eq. (E4) is expressed as

$$x_{\mathrm{crit}} = \frac{8L}{3\sqrt{3}\pi}\sqrt{\frac{\sigma}{QY}}, \tag{J6}$$

with Q the mechanical quality factor. The critical amplitude is linearly proportional to the resonator size L. The critical energy E_{crit} associated with reaching this critical amplitude is given by

$$E_{\mathrm{crit}} = \frac{1}{2}kx_{\mathrm{crit}}^2 = \frac{16L^2h\sigma^2}{27QY}. \tag{J7}$$

This energy scales with the resonator area L^2 and thickness h, underscoring the merits of miniaturization. A large Young's modulus is also beneficial, as it increases the Duffing nonlinearity [which arises in response to an elongation of the material—see Eq. (B11)] and therefore reduces the critical energy. Reducing the tensile stress σ also reduces the critical energy, at a cost of a reduced operational frequency and reduced impedance mismatch between the suspended membrane and the substrate, leading to increased acoustic radiative losses.

As an example, here we estimate the prospects for miniaturization of our platform considering a resonator made of a membrane with thickness as low as 10 nm and tensile stress $\sigma \sim 10$ MPa.

We use Eq. (J7) to estimate the potential energy-cost reduction for nonlinear nanomechanical logic. A significant step forward can be achieved with use of a resonator made of a Si_3N_4 membrane with thickness of 10 nm and tensile stress $\sigma \sim 10$ MPa and a Q factor of approximately 4000. With these feasible parameters, our platform would operate at the Landauer limit, having a resonance frequency of approximately 180 MHz and speed of gate operations of approximately 50 kHz. The ultimate reduction in thickness can be achieved through the use of a purely 2D nanomechanical resonator, made from a 2D material such as graphene [60–66], or molybdenum disulfide (MoS_2) [67]. Such materials have been used to build high-Q suspended-membrane resonators exhibiting hardening Duffing nonlinearity [65,67], and are therefore compatible with our scalable approach to nanomechanical computing.

We consider a square single-layer graphene drum resonator operating at the Landauer limit with critical energy $E_{\mathrm{crit}} = \ln(2)k_BT$. The required parameters for this resonator are the Young's modulus, the size, and the Q factor and their values are compared with the values for our current platform in Table II.

In Fig. 11 we plot the predicted operating frequency [Fig. 11(a)], speed of gate operations given by the dissipation rate [Fig. 11(b)], and the minimum required quality factor [Fig. 11(c)], all for a nanomechanical logic gate based on a single-layer graphene membrane. These predictions are calculated for three different intrinsic stresses and as a function of the size of the graphene drum. For the case where the drum size L is 100 nm, Eqs. (J2), (J5), and (J7) predict a resonator with a resonance frequency of approximately 20 GHz and gate speed in the region of approximately 100 MHz. These calculations were done with a Young's modulus for graphene on the order of 1 TPa [60–62,65], density $\rho_{2\mathrm{D}} = 8 \times 10^{-19}$ kg/μm^2 [63,64] for single-layer graphene, thickness $h = 0.3$ nm, and tensile stress σ up to 250×10^6 Pa (consistent with the literature [42,68]).

All parameters are summarized in Table II. This change in resonator design leads to a significant reduction in E_{crit} on the order of 7×10^6, down to a value of

TABLE II. Physical parameters. Young's modulus, the size, and the Q factor for Si_4N_3 are determined from our current experimental system, whereas for the graphene membrane, they are chosen as feasible experimental values for platform miniaturization. The rest of the parameters are derived here from Eqs. (J4), (J6), and (J7). These parameters are represented as dashed lines in Fig. 11, calculated assuming a square membrane resonator. These values are in good agreement with those derived from FEM simulations. The small differences arise from the presence of the tunnel barriers, which modify the mode shape, which is not taken into account here.

Parameter	Symbol	Meshed Si_4N_3 membrane	Graphene membrane	Unit abbreviation
Young's modulus	Y	250	1000	GPa
Size	L	80	0.1	μm
Quality factor	Q	28 000	60	NA
Resonance frequency	$\Omega_m/2\pi$	4.1	20 000	MHz
Duffing coefficient	α	2.6×10^{13}	4.1×10^{17}	N/m^3
Critical amplitude	x_{crit}	15×10^{-9}	1×10^{-10}	m
Critical energy	E_{crit}	2.6×10^{-14}	1.23×10^{-21}	J
Critical energy	E_{crit}	7.2×10^6	log(2)	k_BT

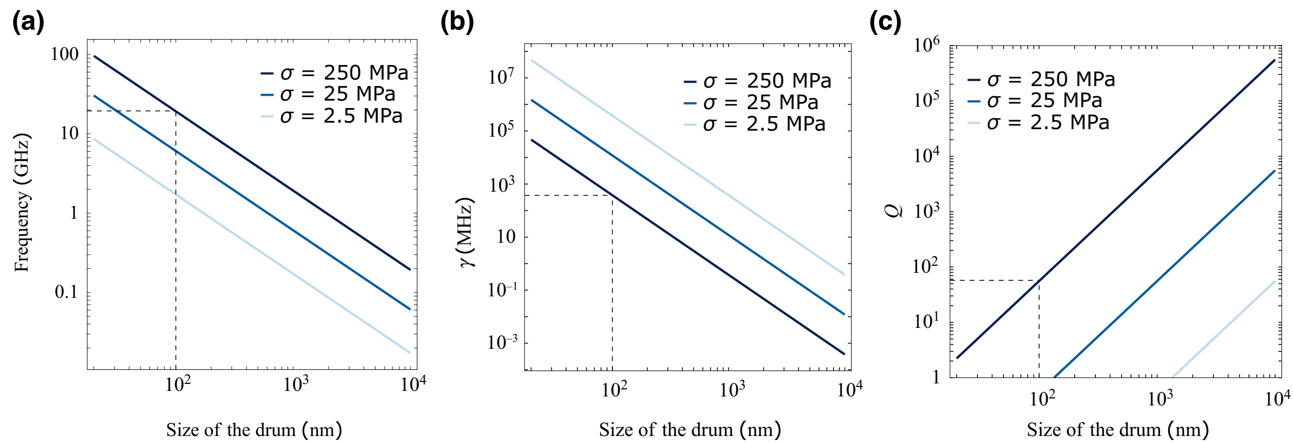

FIG. 11. Graphene-drum resonator operating at the Landauer limit. (a) Operating frequency of a graphene drum as a function of the drum size. (b) Dissipation rate of the drum resonator, and therefore the maximum gate speed. (c) Lower bound for operation at the Landauer limit for the quality factor of the graphene drum as a function of the drum size. The three cases presented correspond to intrinsic stress σ of 2.5, 25, and 250 MPa.

only $0.7k_BT$, reaching the Landauer limit for irreversible computing [6].

Interestingly, in this regime, the mechanical resonance frequency is sufficiently high to allow passive cooling of the mechanical resonator into its quantum ground state with use commercial cryogenic systems. Our computing architecture could also then be used as a coherent Ising machine to solve nondeterministic-polynomial-time-hard computing problems [69], or potentially even as the basis for a purely nanomechanical quantum computer.

APPENDIX K: SYNCHRONIZATION DEMANDS

The use of resonator-based logic at large scale presents a formidable phase-synchronization challenge. In our approach, stable operation requires that the electrical pumps and acoustic inputs of each gate are phase synchronized within a narrow range. This is complicated by the nonlinear response of the resonator, which introduces intensity-dependent phase shifts [30]. However, the phases of the outputs are easily predictable and reliable as shown by our simulations and the robustness of our NAND gate. Therefore, for a nanomechanical circuit composed of tens of gates, such as a flip-flop, a full adder, or a multiplier, the phase between each gate can be adjusted by one carefully choosing the acoustic path length between gates. Additionally, we successfully performed a three-gate logic circuit simulation (not shown here), achieving three-bit logic operation, thus validating that phase shifts due to nonlinear response do not preclude cascaded logic. Nevertheless, scale-up will require precise engineering of both acoustic paths and electrical phases, and may also require analog electrical control. There is also an idea that neatly sidesteps the need for phase synchronization. Our architecture is compatible with parametron computing, which has been demonstrated with use of coupled parametric electrical [70] and electromechanical [71] resonators. Parametronic computing uses parametric nonlinearities that are accessible in our resonators, and can greatly expand the stable regime of operation, while also enabling straightforward feedback prevention [70].

[1] M. Horowitz, in *2014 IEEE International Solid-State Circuits Conference Digest of Technical Papers (ISSCC)* (IEEE, San Francisco, CA, USA, 2014), p. 10.
[2] S. Manipatruni, D. E. Nikonov, and I. A. Young, Beyond CMOS computing with spin and polarization, Nat. Phys. **14**, 338 (2018).
[3] S. Manipatruni, D. E. Nikonov, C.-C. Lin, T. A. Gosavi, H. Liu, B. Prasad, Y.-L. Huang, E. Bonturim, R. Ramesh, and I. A. Young, Scalable energy-efficient magnetoelectric spin–orbit logic, Nature **565**, 35 (2019).
[4] A. Danowitz, K. Kelley, J. Mao, J. P. Stevenson, and M. Horowitz, CPU DB: Recording microprocessor history, Commun. ACM **55**, 55 (2012).
[5] J. D. Meindl, Q. Chen, and J. A. Davis, Limits on silicon nanoelectronics for terascale integration, Science **293**, 2044 (2001).
[6] R. Landauer, Irreversibility and heat generation in the computing process, IBM J. Res. Dev. **5**, 183 (1961).
[7] J. Goetz, Sensors that can take the heat, part 1: Opening the high-temperature toolbox, Sensors: J. Appl. Sens. Technol. **17**, 20 (2000).
[8] A. Hassan, Y. Savaria, and M. Sawan, Electronics and packaging intended for emerging harsh environment applications: A review, IEEE Trans. Very Large Scale Integr. Syst. **26**, 2085 (2018).
[9] M. Roukes, in *IEDM Technical Digest. IEEE International Electron Devices Meeting, 2004* (IEEE, San Francisco, CA, USA, 2004), p. 539.
[10] D. N. Guerra, A. R. Bulsara, W. L. Ditto, S. Sinha, K. Murali, and P. Mohanty, A noise-assisted reprogrammable

nanomechanical logic gate, Nano Lett. **10**, 1168 (2010).
[11] T.-H. Lee, S. Bhunia, and M. Mehregany, Electromechanical computing at 500 °C with silicon carbide, Science **329**, 1316 (2010).
[12] Y. Song, R. M. Panas, S. Chizari, L. A. Shaw, J. A. Jackson, J. B. Hopkins, and A. J. Pascall, Additively manufacturable micro-mechanical logic gates, Nat. Commun. **10**, 882 (2019).
[13] H. Yasuda, P. R. Buskohl, A. Gillman, T. D. Murphey, S. Stepney, R. A. Vaia, and J. R. Raney, Mechanical computing, Nature **598**, 39 (2021).
[14] O. R. Bilal, A. Foehr, and C. Daraio, Bistable metamaterial for switching and cascading elastic vibrations, Proc. Natl. Acad. Sci. USA **114**, 4603 (2017).
[15] H. Yasuda, T. Tachi, M. Lee, and J. Yang, Origami-based tunable truss structures for non-volatile mechanical memory operation, Nat. Commun. **8**, 962 (2017).
[16] B. Treml, A. Gillman, P. Buskohl, and R. Vaia, Origami mechanologic, Proc. Natl. Acad. Sci. **115**, 6916 (2018).
[17] I. Mahboob, H. Okamoto, and H. Yamaguchi, An electromechanical Ising Hamiltonian, Sci. Adv. **2**, e1600236 (2016).
[18] M. H. Matheny, J. Emenheiser, W. Fon, A. Chapman, A. Salova, M. Rohden, J. Li, M. Hudoba de Badyn, M. Pósfai, L. Duenas-Osorio, M. Mesbahi, J. P. Crutchfield, M. C. Cross, R. M. D'Souza, and M. L. Roukes, Exotic states in a simple network of nanoelectromechanical oscillators, Science **363**, eaav7932 (2019).
[19] J.-S. Wenzler, T. Dunn, T. Toffoli, and P. Mohanty, A nanomechanical Fredkin gate, Nano Lett. **14**, 89 (2014).
[20] E. A. Wollack, A. Y. Cleland, R. G. Gruenke, Z. Wang, P. Arrangoiz-Arriola, and A. H. Safavi-Naeini, Quantum state preparation and tomography of entangled mechanical resonators, Nature **604**, 463 (2022).
[21] U. von Lüpke, Y. Yang, M. Bild, L. Michaud, M. Fadel, and Y. Chu, Parity measurement in the strong dispersive regime of circuit quantum acoustodynamics, Nat. Phys. **18**, 794 (2022).
[22] C. Chamberland, K. Noh, P. Arrangoiz-Arriola, E. T. Campbell, C. T. Hann, J. Iverson, H. Putterman, T. C. Bohdanowicz, S. T. Flammia, A. Keller, G. Refael, J. Preskill, L. Jiang, A. H. Safavi-Naeini, O. Painter, and F. G. Brandão, Building a fault-tolerant quantum computer using concatenated cat codes, PRX Quantum **3**, 010329 (2022).
[23] R. L. Badzey, G. Zolfagharkhani, A. Gaidarzhy, and P. Mohanty, A controllable nanomechanical memory element, Appl. Phys. Lett. **85**, 3587 (2004).
[24] Z. A. Ye, S. Almeida, M. Rusch, A. Perlas, W. Zhang, U. Sikder, J. Jeon, V. Stojanović, and T.-J. K. Liu, in *2018 IEEE International Electron Devices Meeting (IEDM)* (IEEE, San Francisco, CA, USA, 2018), p. 4.1.1, ISSN: 2156-017X.
[25] Y. Perrin, A. Galisultanov, L. Hutin, P. Basset, H. Fanet, and G. Pillonnet, Contact-free MEMS devices for reliable and low-power logic operations, IEEE Trans. Electron Devices **68**, 2938 (2021).
[26] I. Mahboob, E. Flurin, K. Nishiguchi, A. Fujiwara, and H. Yamaguchi, Interconnect-free parallel logic circuits in a single mechanical resonator, Nat. Commun. **2**, 198 (2011).
[27] D. Hatanaka, T. Darras, I. Mahboob, K. Onomitsu, and H. Yamaguchi, Broadband reconfigurable logic gates in phonon waveguides, Sci. Rep. **7**, 12745 (2017).
[28] D. Hatanaka, I. Mahboob, K. Onomitsu, and H. Yamaguchi, A phonon transistor in an electromechanical resonator array, Appl. Phys. Lett. **102**, 213102 (2013).
[29] S. Ilyas, S. Ahmed, M. A. A. Hafiz, H. Fariborzi, and M. I. Younis, Cascadable microelectromechanical resonator logic gate, J. Micromech. Microeng. **29**, 015007 (2019).
[30] T. Jin, C. G. Baker, E. Romero, N. P. Mauranyapin, T. M. F. Hirsch, W. P. Bowen, and G. I. Harris, Cascading of nanomechanical resonator logic, Int. J. Unconv. Comput. **18**, 49 (2023).
[31] D. Hatanaka, I. Mahboob, K. Onomitsu, and H. Yamaguchi, Phonon waveguides for electromechanical circuits, Nat. Nanotechnol. **9**, 520 (2014).
[32] E. Romero, R. Kalra, N. P. Mauranyapin, C. G. Baker, C. Meng, and W. P. Bowen, Propagation and imaging of mechanical waves in a highly stressed single-mode acoustic waveguide, Phys. Rev. Appl. **11**, 064035 (2019).
[33] T. M. F. Hirsch, N. P. Mauranyapin, E. Romero, X. Jin, G. Harris, C. G. Baker, and W. P. Bowen, Directional emission in an on-chip acoustic waveguide, Appl. Phys. Lett. **124**, 013504 (2024).
[34] Y. Tadokoro and H. Tanaka, Highly sensitive implementation of logic gates with a nonlinear nanomechanical resonator, Phys. Rev. Appl. **15**, 024058 (2021).
[35] N. P. Mauranyapin, E. Romero, R. Kalra, G. Harris, C. G. Baker, and W. P. Bowen, Tunneling of transverse acoustic waves on a silicon chip, Phys. Rev. Appl. **15**, 054036 (2021).
[36] S. Schmid, L. G. Villanueva, and M. L. Roukes, *Fundamentals of Nanomechanical Resonators* (Springer International Publishing, Cham, 2016).
[37] C. Bekker, C. G. Baker, R. Kalra, H.-H. Cheng, B.-B. Li, V. Prakash, and W. P. Bowen, Free spectral range electrical tuning of a high quality on-chip microcavity, Opt. Express **26**, 33649 (2018).
[38] J. Cha and C. Daraio, Electrical tuning of elastic wave propagation in nanomechanical lattices at MHz frequencies, Nat. Nanotechnol. **13**, 1016 (2018).
[39] J. Cha, K. W. Kim, and C. Daraio, Experimental realization of on-chip topological nanoelectromechanical metamaterials, Nature **564**, 229 (2018).
[40] M. J. Brennan, I. Kovacic, A. Carrella, and T. P. Waters, On the jump-up and jump-down frequencies of the Duffing oscillator, J. Sound Vib. **318**, 1250 (2008).
[41] V. Zhirnov, R. Cavin, and L. Gammaitoni, in *ICT—Energy—Concepts Towards Zero—Power Information and Communication Technology*, edited by G. Fagas (InTech, Rijeka, Croatia, 2014).
[42] G. López-Polín, C. Gómez-Navarro, V. Parente, F. Guinea, M. Katsnelson, F. Pérez-Murano, and J. Gómez-Herrero, Increasing the elastic modulus of graphene by controlled defect creation, Nat. Phys. **11**, 26 (2015).
[43] M. Jung, P. Rickhaus, S. Zihlmann, A. Eichler, P. Makk, and C. Schönenberger, GHz nanomechanical resonator in an ultraclean suspended graphene *p–n* junction, Nanoscale **11**, 4355 (2019).

[44] B. Xu, P. Zhang, J. Zhu, Z. Liu, A. Eichler, X.-Q. Zheng, J. Lee, A. Dash, S. More, S. Wu, Y. Wang, H. Jia, A. Naik, A. Bachtold, R. Yang, P. X.-L. Feng, and Z. Wang, Nanomechanical resonators: Toward atomic scale, ACS Nano **16**, 15545 (2022).
[45] R. Lifshitz and M. C. Cross, in *Reviews of Nonlinear Dynamics and Complexity*, edited by H. G. Schuster (Wiley-VCH Verlag GmbH & Co. KGaA, Weinheim, Germany, 2008).
[46] K. Liu, Y. Sun, F. Zheng, M.-Y. Tse, Q. Sun, Y. Liu, and J. Hao, A general strategy to achieve colossal permittivity and low dielectric loss through constructing insulator/semiconductor/insulator multilayer structures, J. Low Temp. Phys. **192**, 346 (2018).
[47] Y. Sun, D. Wu, K. Liu, and F. Zheng, Colossal permittivity and low dielectric loss of thermal oxidation single-crystalline Si wafers, Materials **12**, 1102 (2019).
[48] C. Baker, S. Stapfner, D. Parrain, S. Ducci, G. Leo, E. M. Weig, and I. Favero, Optical instability and self-pulsing in silicon nitride whispering gallery resonators, Opt. Express **20**, 29076 (2012).
[49] M. Kurosu, D. Hatanaka, K. Onomitsu, and H. Yamaguchi, On-chip temporal focusing of elastic waves in a phononic crystal waveguide, Nat. Commun. **9**, 1331 (2018).
[50] W. Fu, Z. Shen, Y. Xu, C.-L. Zou, R. Cheng, X. Han, and H. X. Tang, Phononic integrated circuitry and spin–orbit interaction of phonons, Nat. Commun. **10**, 2743 (2019).
[51] T. Faust, P. Krenn, S. Manus, J. Kotthaus, and E. Weig, Microwave cavity-enhanced transduction for plug and play nanomechanics at room temperature, Nat. Commun. **3**, 728 (2012).
[52] C. Chen, S. Rosenblatt, K. I. Bolotin, W. Kalb, P. Kim, I. Kymissis, H. L. Stormer, T. F. Heinz, and J. Hone, Performance of monolayer graphene nanomechanical resonators with electrical readout, Nat. Nanotech. **4**, 861 (2009).
[53] X. Song, M. Oksanen, M. A. Sillanpää, H. G. Craighead, J. M. Parpia, and P. J. Hakonen, Stamp transferred suspended graphene mechanical resonators for radio frequency electrical readout, Nano Lett. **12**, 198 (2012).
[54] M. Aspelmeyer, T. J. Kippenberg, and F. Marquardt, *Cavity Optomechanics: Nano-And Micromechanical Resonators Interacting with Light* (Springer, Berlin, 2014).
[55] Note that Ref. [10] reports operations at $10k_BT_{\mathrm{eff}}$, where T_{eff} is the effective temperature of the device. This is around 10^3T, corresponding to an energy cost of $2 \times 10^4 k_BT$.
[56] S. Ilyas, M. A. A. Hafiz, S. Ahmed, H. Fariborzi, and M. I. Younis, Toward cascadable microelectromechanical resonator logic units based on second vibration modes, AIP Adv. **8**, 105126 (2018).
[57] C. Bekker, R. Kalra, C. Baker, and W. P. Bowen, Injection locking of an electro-optomechanical device, Optica **4**, 1196 (2017).
[58] N. C. Zambon, S. Rodriguez, A. Lemaître, A. Harouri, L. Le Gratiet, I. Sagnes, P. St-Jean, S. Ravets, A. Amo, and J. Bloch, Parametric instability in coupled nonlinear microcavities, Phys. Rev. A **102**, 023526 (2020).
[59] L. Bello, M. C. Strinati, E. G. Dalla Torre, and A. Pe'er, Persistent coherent beating in coupled parametric oscillators, Phys. Rev. Lett. **123**, 083901 (2019).
[60] J. S. Bunch, A. M. van der Zande, S. S. Verbridge, I. W. Frank, D. M. Tanenbaum, J. M. Parpia, H. G. Craighead, and P. L. McEuen, Electromechanical Resonators from graphene sheets, Science **315**, 490 (2007).
[61] C. Lee, X. Wei, J. W. Kysar, and J. Hone, Measurement of the elastic properties and intrinsic strength of monolayer graphene, Science **321**, 385 (2008).
[62] J.-U. Lee, D. Yoon, and H. Cheong, Estimation of Young's modulus of graphene by Raman spectroscopy, Nano Lett. **12**, 4444 (2012).
[63] R. A. Barton, I. R. Storch, V. P. Adiga, R. Sakakibara, B. R. Cipriany, B. Ilic, S. P. Wang, P. Ong, P. L. McEuen, J. M. Parpia, and H. G. Craighead, Photothermal self-oscillation and laser cooling of graphene optomechanical systems, Nano Lett. **12**, 4681 (2012).
[64] R. M. Cole, G. A. Brawley, V. P. Adiga, R. De Alba, J. M. Parpia, B. Ilic, H. G. Craighead, and W. P. Bowen, Evanescent-field optical readout of graphene mechanical motion at room temperature, Phys. Rev. Appl. **3**, 024004 (2015).
[65] T. Inoue, Y. Anno, Y. Imakita, K. Takei, T. Arie, and S. Akita, Resonance control of a graphene drum resonator in a nonlinear regime by a standing wave of light, ACS Omega **2**, 5792 (2017).
[66] Z.-Z. Zhang, X.-X. Song, G. Luo, Z.-J. Su, K.-L. Wang, G. Cao, H.-O. Li, M. Xiao, G.-C. Guo, L. Tian, G.-W. Deng, and G.-P. Guo, Coherent phonon dynamics in spatially separated graphene mechanical resonators, Proc. NatL. Acad. Sci. **117**, 5582 (2020).
[67] A. Castellanos-Gomez, R. van Leeuwen, M. Buscema, H. S. J. van der Zant, G. A. Steele, and W. J. Venstra, Single-layer MoS_2 mechanical resonators, Adv. Mater. **25**, 6719 (2013).
[68] X. Fan, F. Forsberg, A. D. Smith, S. Schröder, S. Wagner, H. Rödjegård, A. C. Fischer, M. Östling, M. C. Lemme, and F. Niklaus, Graphene ribbons with suspended masses as transducers in ultra-small nanoelectromechanical accelerometers, Nat. Electron. **2**, 394 (2019).
[69] Y. Okawachi, M. Yu, J. K. Jang, X. Ji, Y. Zhao, B. Y. Kim, M. Lipson, and A. L. Gaeta, Demonstration of chip-based coupled degenerate optical parametric oscillators for realizing a nanophotonic spin-glass, Nat. Commun. **11**, 4119 (2020).
[70] S. Muroga and K. Takashima, The parametron digital computer MUSASINO-1, IRE Trans. Electron. Comput. **EC-8**, 308 (1959).
[71] I. Mahboob and H. Yamaguchi, Bit storage and bit flip operations in an electromechanical oscillator, Nat. Nanotech. **3**, 275 (2008).